Frank *et al.*
Progress in Earth and Planetary Science (2024) 11:34
https://doi.org/10.1186/s40645-024-00641-y

Progress in Earth and Planetary Science

RESEARCH ARTICLE

Open Access

Deformation mechanisms and fluid conditions of mélange shear zones associated with seamount subduction

Madison Frank[1*], Kohtaro Ujiie[1], Ginta Motohashi[1] and Takayoshi Nagaya[2]

Abstract

Lithologic heterogeneity and the presence of fluids have been linked to seamount subduction and collocated with slow earthquakes. However, the deformation mechanisms and fluid conditions associated with seamount subduction remain poorly understood. The exhumed Chichibu accretionary complex on Amami-Oshima Island preserves mélange shear zones composed of mudstone-dominated mélange and basalt–limestone mélange deformed under sub-greenschist facies metamorphism. The mudstone-dominated mélange contains sandstone, siliceous mudstone, and basalt lenses in an illitic matrix. The basalt–limestone mélange contains micritic limestone and basalt lenses in a chloritic matrix derived from the mixing of limestone and basalt at the foot of a seamount. The basalt–limestone mélange overlies the mudstone-dominated mélange, possibly representing a submarine landslide from the seamount onto trench-fill terrigenous sediments. The asymmetric *S–C* fabrics in both mélanges show top-to-SE shear consistent with megathrust-related shear. Quartz-filled shear and extension veins in the mudstone-dominated mélange indicate brittle failure at near-lithostatic fluid pressure and low differential stress. Microstructural observations show that deformation in the mudstone-dominated mélange was accommodated by dislocation creep of quartz and combined quartz pressure solution with frictional sliding of illite, whereas the basalt-limestone mélange was accommodated by frictional sliding of chlorite and dislocation creep of coarse-grained calcite, with possible pressure solution creep and diffusion creep of fine-grained calcite. The mélange shear zones formed in association with seamount subduction record temporal changes in deformation mechanisms, fluid pressure, and stress state during megathrust shear with brittle failure under elevated fluid pressure, potentially linking tremor generation near subducting seamounts.

Keywords Deformation mechanisms, Fluid conditions, Microstructure, Mélange shear zone, Seamount subduction

*Correspondence:
Madison Frank
mfrank@geol.tsukuba.ac.jp
[1] Graduate School of Science and Technology, University of Tsukuba, 1-1-1 Tennodai, Tsukuba, Ibaraki 305-8572, Japan
[2] Department of Environmental Science, Tokyo Gakugei University, 4-1-1 Nukui Kitamachi, Koganei, Tokyo 184-8501, Japan

1 Introduction

Seamounts derived from hot spot volcanism increase seafloor roughness (e.g., Heuret et al. 2012; Nishimura 2014; Wang and Bilek 2014; Tilley et al. 2021; Gase et al. 2023), and seamount subduction promotes lithologic heterogeneity by introducing volcaniclastic and calcareous sediments into the subduction interface (e.g., Harris et al. 2013; Barnes et al. 2020). Subducting seamounts also influence tremor and slow slip events in several margins, including New Zealand (e.g., Todd et al. 2018), Japan (e.g., Nishikawa et al. 2019; Tonegawa et al. 2020), and Costa Rica (e.g., Norabuena et al. 2004; Outerbridge et al. 2010). Compositionally heterogeneous materials associated with seamount subduction are thought to affect the frictional and rheological properties of subduction shear zones (Barnes et al. 2020; Vannucchi et al. 2022). While the deformation processes and mechanisms preserved in sandstone-mudstone mélange shear zones have been well studied (e.g., Fisher and Byrne 1987; Ujiie 2002; Fagereng 2011), the behavior of seamount-related mélange shear zones remains poorly understood. Vannucchi et al. (2022) studied a mélange formed in association with seamount subduction and showed that hydrothermal alteration prior to subduction strengthened the volcaniclastic mélange matrix. They propose the failure of weak basalt lenses in a strong volcaniclastic matrix as the mechanism for tremor. In contrast, Phillips et al. (2020a) suggest that tremor and slow slip are characterized by velocity-weakening altered basalt embedded in a weaker velocity-strengthening argillaceous matrix. Seamount-derived sediments have been suggested to accommodate megathrust shear during seamount subduction (Bonnet et al. 2020; Leah et al. 2022; Barbero et al. 2023), but the deformation processes and mechanisms of megathrust shear are still unknown, particularly in cases where seamounts have subducted deeper into the subduction zone where temperature-dependent viscous deformation may be favored (e.g., Fagereng and Beall 2021; Ando et al. 2023).

In this paper, we aim to define the lithology, structural characteristics, fluid conditions, and deformation mechanisms preserved in an exhumed accretionary complex associated with seamount subduction on Amami-Oshima Island, Ryukyu Arc. We describe an outcrop of the Chichibu accretionary complex that contains two mélange shear zones: one composed of limestone mixed with seamount-derived basalt, and one dominated by terrigenous sediments. From field and microstructural observations and Raman spectra of carbonaceous materials, we determined the deformation styles and mechanisms recorded in each mélange shear zone and examined temporal changes in fluid pressure and stress state during seamount subduction to sub-greenschist facies metamorphic conditions. We also try to relate the deformation in the mélange shear zones to tremor associated with seamount subduction.

2 Geological setting

Amami-Oshima Island is located in the central Ryukyu Arc, which lies between the Tokara Strait to the north and the Kerama Gap to the south (Fig. 1a). Basement rocks of the island consist of the Eocene Wano Formation and Shimanto accretionary complex in the east and the Chichibu accretionary complex in the west, separated by the Butsuzo Tectonic Line (Osozawa 1984; Takeuchi 1993; Osozawa et al. 2009) (Fig. 1b). The Shimanto and Chichibu accretionary complexes in Amami-Oshima Island are the southwestern extension of the southernmost part of the Shimanto Belt and the Chichibu Belt in the Outer Zone of Southwest Japan (Taira et al. 2016; Wallis et al. 2020).

The Chichibu accretionary complex on Amami-Oshima Island is a mélange characterized by lenses of siliceous mudstone, sandstone, chert, limestone, and basalt in a mudstone matrix (Osozawa 1984). Limestone contains fusulinid, coral, and conodont fossils of Carboniferous to Permian ages, while interbedded limestone and chert contain Triassic radiolarians (Osozawa 1984). Basaltic rocks include pillow lava, breccia, and hyaloclastite (Takeuchi 1993). Geochemical analysis indicates that the basaltic rocks were derived from oceanic island basalt (Motohashi et al. 2023b). The lithological assemblage constituting the mélange, the ages of limestone and chert, and the geochemical characteristics of basalt in the Chichibu accretionary complex on Amami-Oshima Island are well correlated with those in the southernmost part of the Chichibu Belt in the Outer Zone of Southwest Japan, which are interpreted to represent the accretion of a seamount chain along the subduction zone (Matsuoka 1992). The ages of the terrigenous sandstone and mudstone in the Chichibu accretionary complex on Amami-Oshima Island remain unknown, but the correlations of the Chichibu accretionary complex between Amami-Oshima and the Outer Zone of Southwest Japan suggest a Late Jurassic to Early Cretaceous accretionary age (Takeuchi 1993).

The Shimanto accretionary complex on Amami-Oshima Island consists of mudstone and sandstone intercalated with basalt, hemipelagic mudstone, and silicic tuffs (Osozawa 1984; Osozawa et al. 2009). The accretionary age was Early to Middle Cretaceous based on radiolarians and ammonites in terrigenous sediments (Ishikawa and Yamakuchi 1965; Osozawa 1984; Matsumoto et al. 1966). At the easternmost edge of the island, Eocene Wano Formation composed of sandstone and conglomerate containing basalt, chert, and marl is exposed (Osozawa 1984).

The Chichibu accretionary complex was exhumed above the Shimanto accretionary complex by the Butsuzo Tectonic Line. Osozawa et al. (2009) identified outcrop-scale out-of-sequence thrust faults in the Chichibu accretionary complex. Otherwise, no widespread exhumation-related structures have been identified in the Chichibu accretionary complex.

Several intrusive rocks have been identified on Amami-Oshima Island. Small granitic bodies of Eocene age have intruded the Shimanto accretionary complex (Shibata and Nozawa 1966). Middle Cretaceous camptonite and spessartite lamprophyres with chemical characteristics representative of ocean island basalt have been identified in both the Chichibu and Shimanto accretionary complexes (Kanisawa et al. 1983; Osozawa 1984). Recently, middle Miocene alkaline basalt representative of forearc alkaline magmatism was reported from Amami-Oshima Island (Motohashi et al. 2023a).

3 Methods

Thirty-nine samples were collected from the various lithologies of the Chichibu accretionary complex for petrological, microstructural, and Raman spectroscopic analyses. Forty-six thin sections cut parallel to lineation and perpendicular to foliation were made from the collected samples.

3.1 SEM and EDS analysis

Field emission scanning electron microscopy (SEM) and energy-dispersive X-ray spectroscopy (EDS) analyses were conducted at the University of Tsukuba using a JEOL JSM-IT300HR scanning electron microscope to investigate microstructures and mineral composition. Thin sections were coated with carbon prior to analysis to prevent charging. EDS mapping was conducted under a high vacuum using an accelerating voltage of 15 kV, a working distance of 10 mm, and a beam current of 60–70 μA.

3.2 EBSD analysis

Electron backscatter diffraction (EBSD) data were collected from a representative sample of a micritic limestone lens to investigate the grain size, intragrain distortion, and crystallographic preferred orientations (CPO) of the calcite. The thin section was polished with diamond pastes of progressively finer sizes (0.25 μm at minimum) and finally with colloidal silica. EBSD analysis was conducted at the University of Tokyo using a JEOL JSM-6510LV scanning electron microscope and Oxford Aztec software. The operating conditions were as follows: 10 kV accelerating voltage and 24–25 mm working distance. Data were collected in a low vacuum (10 Pa) at ×40 magnification.

EBSD mapping was carried out using a step size of 1 μm over 516,683 pixels. Automatic indexing of calcite ($a=b=4.97$ Å, $c=16.96$ Å, and $\beta=120°$; Paquette and Reeder 1990) and chlorite ($a=5.24$ Å, $b=9.07$ Å,

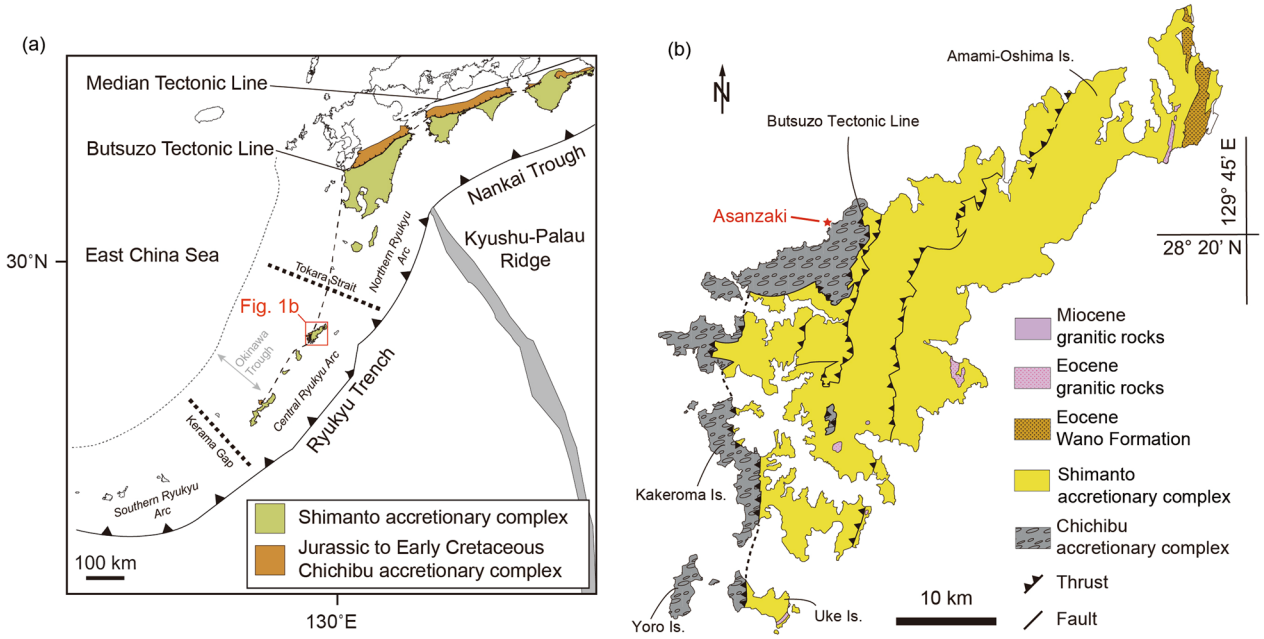

Fig. 1 Tectonic setting and geological map of Amami-Oshima Island. Modified from Motohashi et al. (2023a, 2023b). **a** Distribution of the Shimanto and Chichibu accretionary complexes in southwest Japan and the Ryukyu Arc. Amami-Oshima Island (red box) is located within the central Ryukyu Arc. **b** Geological map of Amami-Oshima Island (modified from Takeuchi 1993). The field area, Asanzaki, is highlighted in red

$c = 14.29$ Å, and $\beta = 97.0°$; Eggleston and Bailey 1967) grains was performed using up to 12 Kikuchi bands, a Hough resolution of 60, and mean angular deviation (MAD) values less than 2.0°. Quantitative analyses of EBSD data, including map analyses (e.g., grain reconstruction, grain size, and misorientation), CPO pole figures, and orientation distribution functions (e.g., M-index), were carried out using the MTEX toolbox for MATLAB (Hielscher and Schaeben 2008; Mainprice et al. 2014). Grain boundaries were constructed using a misorientation threshold criterion of 10 degrees, and grains of isolated indexed points with ≤ 3 pixels were excluded. Grain orientation spread (GOS) of calcite was defined as the intragranular misorientation for a given pixel within each of the calcite grains relative to the mean orientation of the parent calcite grain. CPO patterns of calcite were calculated using a dataset of the mean orientations of each calcite grain constructed based on EBSD indexing to reduce any influence by large grains. In this study, no significant change in calcite CPO patterns due to data filtering conditions using MAD was observed. CPO fabric strength was assessed using the M-index (Skemer et al. 2005). All other methods of the EBSD analyses followed Nagaya et al. (2017).

3.3 Raman spectroscopic analysis

Three mudstone samples were collected with ~ 50 m spacing to determine the peak temperature from Raman spectroscopic analysis of carbonaceous material. Samples were analyzed at Nagoya University using a Nicolet Almega XR (Thermo Scientific, Yokohama, Japan) with a 532 nm Nd-YAG laser passed through a confocal microscope (Olympus, BX51: Olympus, Tokyo, Japan) with a 100× objective (Olympus Mplan-BD 100X, NA = 0.90). To avoid influence from mechanical polishing, carbon grains embedded within transparent minerals were targeted in standard petrographic thin sections and irradiated for 30 s with a 1–3 mW laser. Forty carbon grains were measured per sample.

Raman spectra peaks were fitted using the methodology described by Kouketsu et al. (2014). Spectral peak patterns were manually analyzed initially to identify the best fit of G-, D1-, D2-, D3-, and D4-bands following the flowchart in Kouketsu et al. (2014). After the initial manual peak fitting, the spectra were automatically decomposed using PeakFit v4.12 (Systat Software Inc.). We corrected the Raman spectra by subtracting a linear baseline in the range of 1000–1800 cm^{-1}, and then the spectra were decomposed with a Gaussian–Lorentzian Sum Voigt function. In all cases, the D4-band was fixed at 1245 cm^{-1}, and peak width and shape were allowed to vary. In measurements where the D1-band peak shape was asymmetric (i.e., Fitting F of Kouketsu et al. 2014), the G-band was fixed at 1593 cm^{-1} with a Lorentz function. Temperatures were calculated using the full width at half maximum of the D1-band (FWHM-D1):

$$T\ (°C) = -2.15 \times (\text{FWHM - D1}) + 478. \quad (1)$$

Values exceeding 2× the standard deviation (σ) were identified as outliers and excluded prior to calculation of the mean temperature.

4 Results

4.1 Field observations

The study area is located in Asanzaki, in the northwestern part of Amami-Oshima Island (Fig. 1b), where the outcrop is most laterally accessible. Here, two types of mélanges are recognized in the Chichibu accretionary complex: basalt–limestone mélange (BLM) and mudstone-dominated mélange (MDM) (Fig. 2a). The BLM is distributed in the northwest and intruded by basaltic sills along the westernmost margin. The MDM is distributed in the southeast and cut by a series of minor NW-dipping thrust faults. The shear direction of the thrust faults, determined by quartz slickenfiber steps, is top-to-SE or ESE reverse shear with one exception showing top-to-S shear (Fig. 2b). No thrust faults are observed within the BLM. Foliations in the BLM and MDM are parallel; both dip moderately WNW (Fig. 3a). The BLM overlies the MDM, and the contact between the BLM and MDM is parallel to foliations in the BLM and MDM (Fig. 3b). The characteristics of the BLM and MDM are described below.

4.1.1 Basalt–limestone mélange (BLM)

The BLM is characterized by lenses of micritic limestone and basalt in a green-gray matrix (Fig. 3c). The minimum thickness of the BLM, limited by outcrop exposure, is 18 m. Lenses in the BLM are subangular to subrounded, with a long axis of 0.05–20 m. The proportion of limestone to basalt in the matrix varies across the outcrop, from sections of limestone with almost no macroscopic basalt lenses observable to zones with an approximately 4:1 limestone/basalt lens ratio. Basaltic pillow lava and breccia and interbedded calcareous mudstone/greenstone exist locally in the BLM (Fig. 2a). Bedding in interbedded calcareous mudstone/greenstone is approximately parallel to the foliation of the BLM but locally folded. The matrix of the BLM is well foliated and characterized by anastomosing polished surfaces with slickenlines showing scattered trends (Fig. 3d, f). Limestone and basalt lenses are surrounded by matrix foliation (Fig. 3e) and locally elongated parallel to the foliation. In places, asymmetric lenses and the matrix foliations show *S*–*C* fabric consistent with top-to-SE shear sense (Fig. 3c). *S* surfaces, defined by the alignment of matrix foliations

and long axes of basalt and limestone lenses, are cut by *C* surfaces at less than 45°.

Within the BLM, calcite extension and shear veins are rarely observed. Calcite shear veins near-parallel to foliation were identified in outcrops where the matrix is intensely foliated but cannot be traced for more than a few centimeters along their length. Slickenfibers and slickensteps on calcite shear veins indicate top-to-SE or -ESE shear (Fig. 3f). Within individual basalt and micritic limestone lenses, extension veins of < 10 cm in length are observed at various angles to foliation. Extension veins at high angles to the foliation sometimes cross-cut multiple lenses and are displaced by shear surfaces.

Basaltic sills intruding into the BLM have sharp boundaries and display chilled margins. Calcite veins are rarely observed near basaltic sills. Foliations within the sills are subparallel to those in the BLM and the MDM. The geochemical features of the basaltic sills and timing of intrusion suggest that the basaltic sills originated from petit-spot volcanism in the oceanic plate, while other nonintrusive basaltic rocks show geochemical features consistent with hot spot volcanism (Motohashi et al. 2023b).

4.1.2 Mudstone-dominated mélange (MDM)

The MDM is characterized by lenses of sandstone, siliceous mudstone, and basalt in a mudstone matrix (Fig. 4a). The length of the long axis of the lenses ranges from 0.02 to 20 m. The minimum thickness of the MDM is 31 m or thinner, as thrust faults may contribute to repetition of the MDM (Fig. 2a). Matrix foliations are anastomosing and wrap phacoids, showing a scaly fabric. Slickenlines on the polished foliations show a scattered trend (Fig. 4c). Asymmetric lenses and scaly foliations

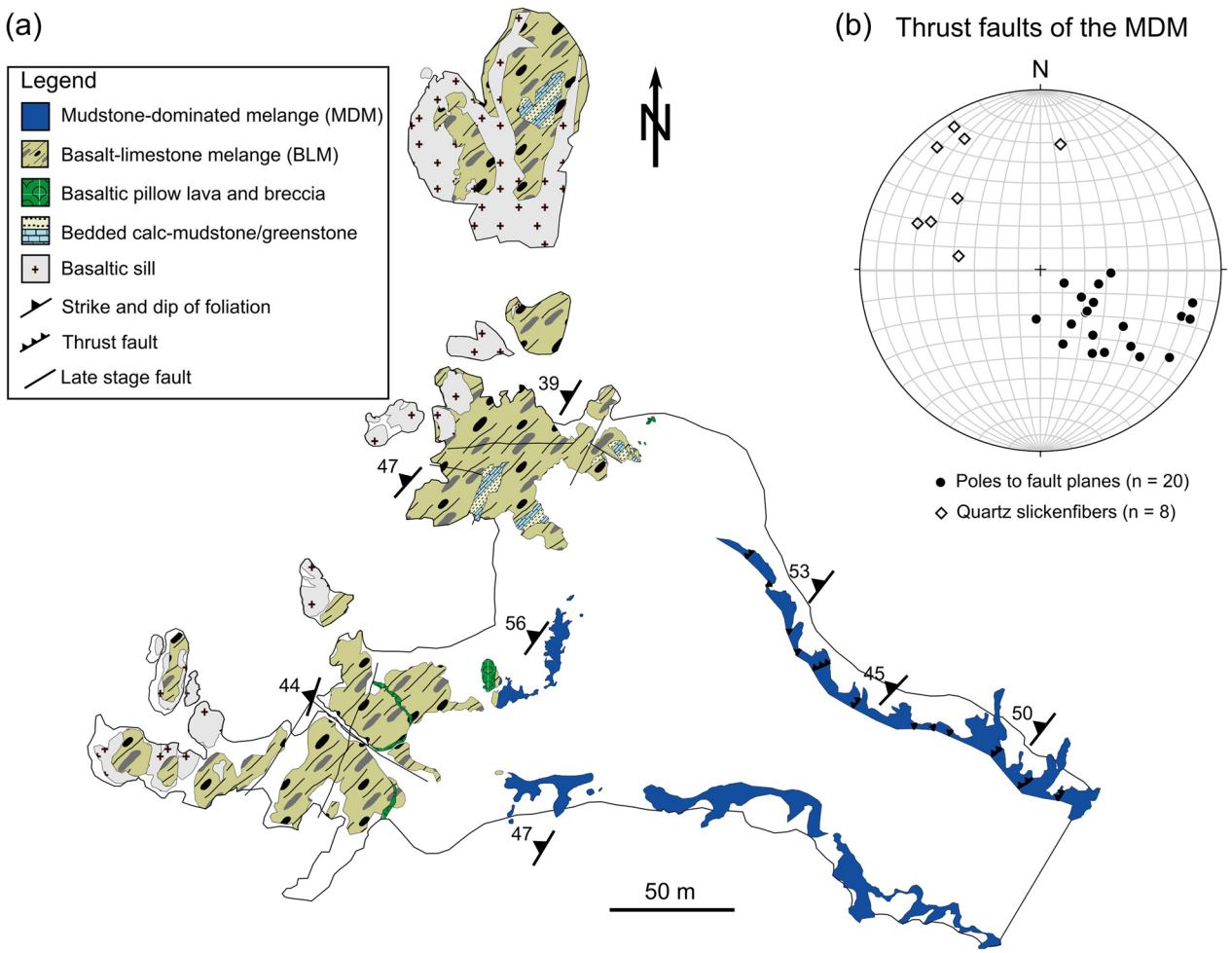

Fig. 2 Geological map of Asanzaki. **a** Geological map showing two types of mélanges. **b** Stereonet showing poles to thrust faults in the MDM (black dots) and quartz slickenfibers (hollow diamonds) on the thrust faults

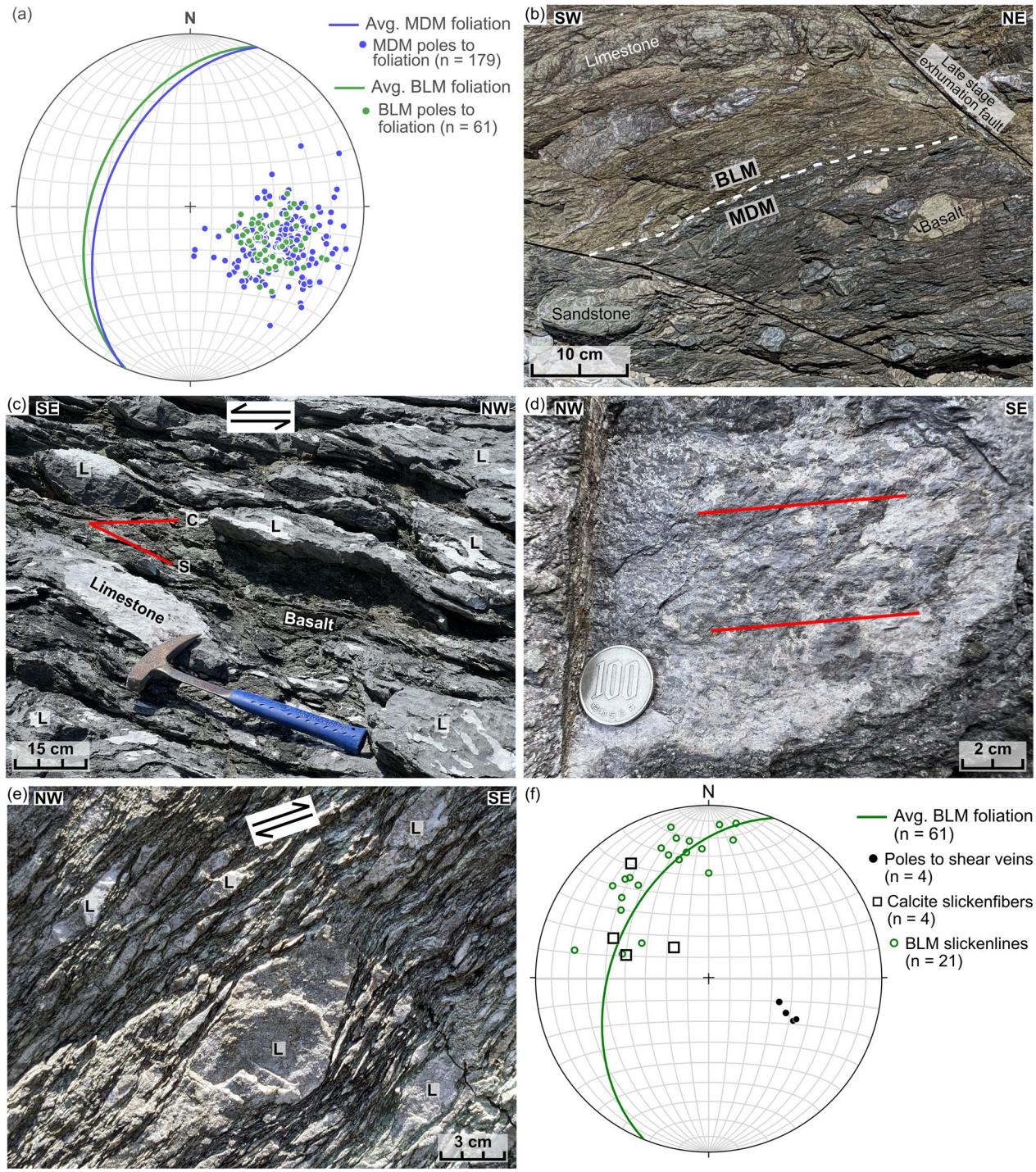

Fig. 3 Basalt–limestone mélange (BLM) at Asanzaki. **a** Stereonet showing poles to foliation and average foliation in BLM (green) and MDM (blue). **b** Contact between the BLM and MDM. **c** BLM: limestone (L) and OIB basalt lenses in a greenish matrix showing *S*–*C* fabric consistent with top-to-SE shear. **d** Polished surface with slickenlines (red lines) in the BLM matrix. White patches on the polished surface are calcite. **e** BLM showing that matrix foliation surrounds gray limestone lenses (L). **f** Stereonet showing average foliation of the BLM (green circle), slickenfibers from calcite shear veins (open box), and slickenlines on polished surfaces (open green circles)

constitute *S*–*C* fabric with top-to-SE shear sense (Fig. 4a). *S* surfaces defined by the alignment of lenses and matrix foliations are transected or deflected by *C* surfaces at less than 45°.

Both quartz-filled extension and shear veins are observed in the MDM. The density of quartz veins varies throughout the MDM with no clear correlation to the presence of thrust faults or the distribution of basaltic or sedimentary lenses. The extension veins at moderate to high angles to the foliation are generally restricted to lenses of sandstone and siliceous mudstone with spacing of 1–2 cm (Fig. 4b). Some extension veins at high angles to the foliation penetrate the mudstone matrix and are displaced by shear surfaces. The extension veins parallel to the foliation or the *S*-surface are laterally continuous for less than 1 m (Fig. 4b, d) and locally underwent sigmoidal deformation associated with top-to-SE viscous shear (Fig. 4f). Shear veins, defined by the presence of slickenfibers (Fig. 4e), develop parallel to the *C*-surface (Fig. 4b). Shear sense, determined from slickenfibers and steps, indicates top-to-SE thrust movement (Fig. 4d).

4.2 Mineral assemblage, microstructures, and temperature conditions

4.2.1 Basalt–limestone mélange (BLM)

Limestone lenses are composed of microcrystalline calcite and radiolarian tests replaced by calcite (Fig. 5a). EBSD mapping of a limestone lens gives an average grain size of 7.8 μm (Fig. 5b) for microcrystalline calcite. Since the proportion of unindexed grains (Fig. 5d), representative of the smallest grain size is high, the average grain size is expected to be overestimated. Microcrystalline calcite has small misorientation angles of mostly < 1–2° (Fig. 5c). The limestone lenses show no chemical zoning. The crystallographic fabric is random (Fig. 5e), with an M-index (Skemer et al. 2005) of 0.01. Albite grains are often observed within limestone lenses.

Basalt lenses are aphyric and composed of fine-grained (< 15 μm) albite with microcrystalline calcite and Fe–Ti oxide minerals (Fig. 5f). The BLM matrix is composed of chlorite with minor illite. Foliations, defined by the alignment of chlorite with lesser illite, wrap limestone and basalt lenses to form an interconnected network or *S*–*C* fabric showing top-to-SE shear sense (Fig. 5f). Fe-Ti oxide minerals and illite are concentrated in dark seams within the chloritic matrix (Fig. 6b). Pressure shadows around calcite or albite grains or chlorite strain shadows around basalt or limestone lenses have not been observed. The chilled margins of intrusive basalt sills contain glassy groundmass that is locally altered to chlorite (Motohashi et al. 2023b), but otherwise there is no mineralogical change in the BLM with respect to sill proximity.

Coarse-grained calcite is restricted to the margins of micritic limestone lenses and extension veins. Extension veins that crosscut both lenses and matrix at moderate to high angles to foliation are displaced by shear surfaces (Fig. 6a). Calcite veins generally consist of blocky, coarse-grained calcite > 40 μm in size (Figs. 5a, 6c). In contrast to microcrystalline calcite, e-twins are widespread in coarse calcite grains and display bulging boundaries (Fig. 6c). Lamellae morphology and width of calcite twins were assessed using optical microscopy to establish the dominant twin type and associated deformation temperatures (Burkhard 1993). Calcite twin morphology is defined by repeated straight twins of 1–10 μm width, corresponding to type II calcite twins formed at temperatures between 150 and 300 °C (Burkhard 1993). We also considered the calcite twin density paleopiezometer where differential stress (σ_d) is calculated from calcite twin density (N_L), the number of twins per mm, using the following equation (Rybacki et al. 2013):

$$\sigma_d = (19.5 \pm 9.8) \times \sqrt{N_L} \quad (2)$$

Twin density was measured in 76 grains from 7 samples across the BLM. The average N_L ranged from 24 to 200, yielding differential stresses between 97 and 276 MPa (Fig. 6d).

4.2.2 Mudstone-dominated mélange (MDM)

The mudstone matrix of the MDM is primarily composed of quartz, albite, illite, and chlorite with lesser calcite and Fe–Ti oxide minerals (Fig. 7a). Illite is the dominant phyllosilicate in the matrix. Albite grains range in size from 15 to 60 μm and display rare twins. Quartz grain size is highly variable; quartz in the mudstone matrix ranges from 15 to 80 μm, while grains in quartz veins can have a long axis of up to 1.5 mm. Quartz grains in the matrix and in veins commonly display undulose extinction, and bulging grain boundaries are present in quartz veins (Fig. 7b). Under the microscope, the quartz-filled foliation-parallel extension veins have a crack-seal texture defined by stylolitized phyllosilicate solid inclusion bands aligned nearly parallel to the vein margins (Fig. 7c). Spacing of solid inclusion bands is variable, but commonly ranges from 0.1 to 0.6 mm. Quartz grains in crack-seal veins are generally blocky (Fig. 7d), but elongated grains with the long axis perpendicular to the vein margin are also observed. In some cases, quartz shear and extension veins are associated with veins of blocky, coarse-grained calcite. Microscopically, *S*–*C* fabric is characterized by *S* surfaces defined by the alignment of lenses and dark seams composed of illite and titanomagnetite with lesser chlorite that is truncated or deflected by the *C* surfaces (Fig. 7e). Pressure shadows of quartz and illite are

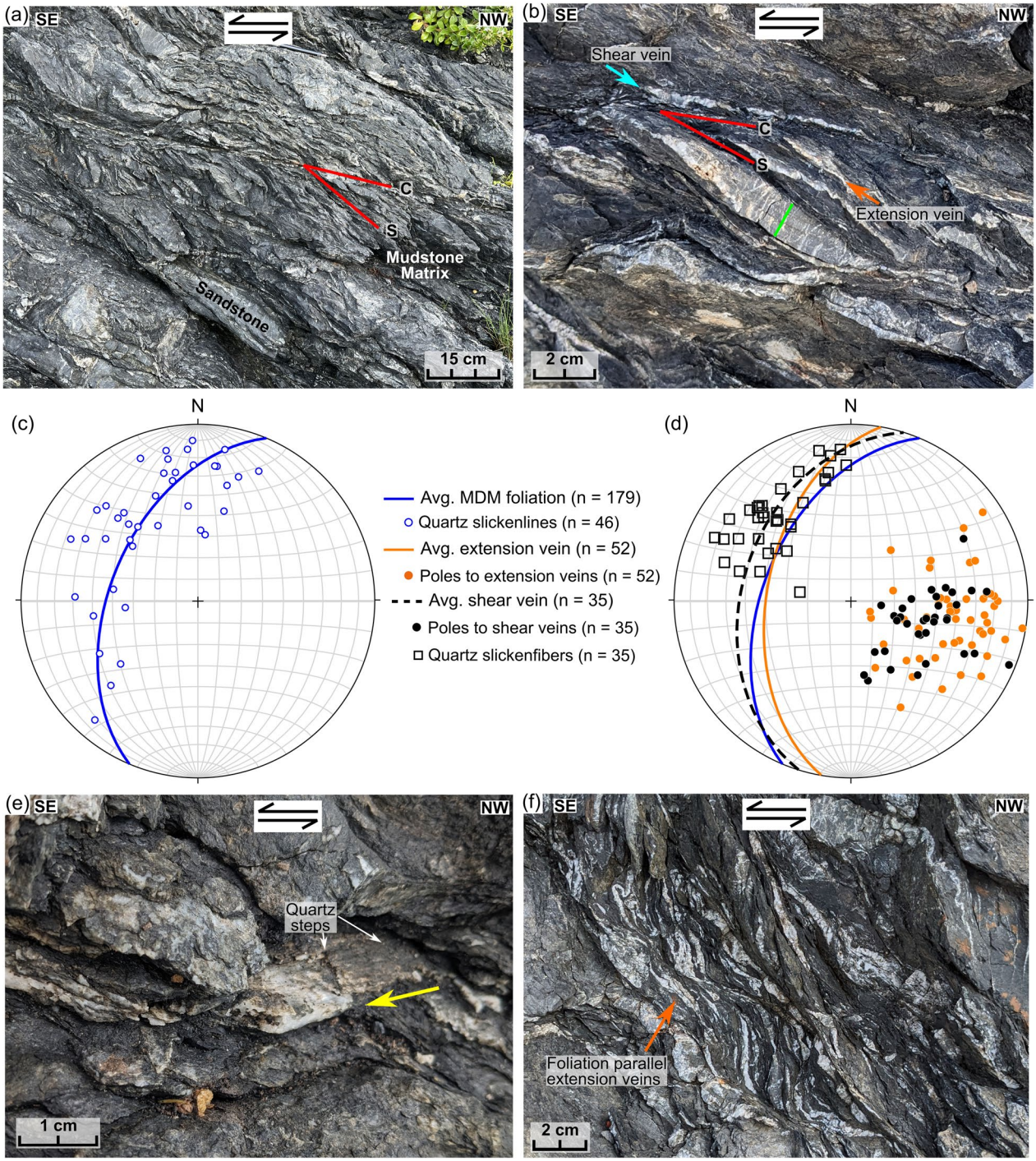

Fig. 4 Mudstone-dominated mélange (MDM) at Asanzaki. **a** Dark, foliated mudstone with siliceous mudstone and sandstone lenses showing *S*–*C* fabric consistent with top-to-SE shear. **b** Quartz extension and shear veins in the MDM. Extension veins at high angles to foliation (green line) are confined to a sandstone lens. The extension veins (orange arrow) are oriented parallel to *S*-surfaces. Extension veins and foliation are cut by the shear vein (blue arrow) parallel to the *C*-surface. **c** Stereonet showing average foliation of the MDM (blue circle) and slickenlines (open blue circles) on polished surfaces. **d** Stereonet showing average foliation of the MDM (blue circle), average shear vein (black dashed circle), and average foliation-parallel extension vein (orange circle). Slickenfibers from quartz shear veins are shown as hollow boxes, poles to foliation-parallel extension veins are shown in orange dots, and poles to shear veins are shown in black dots. **e** Quartz slickenfibers with steps (yellow arrow) on shear vein showing reverse, top-to-SE shear. **f** Viscously deformed foliation-parallel extension veins

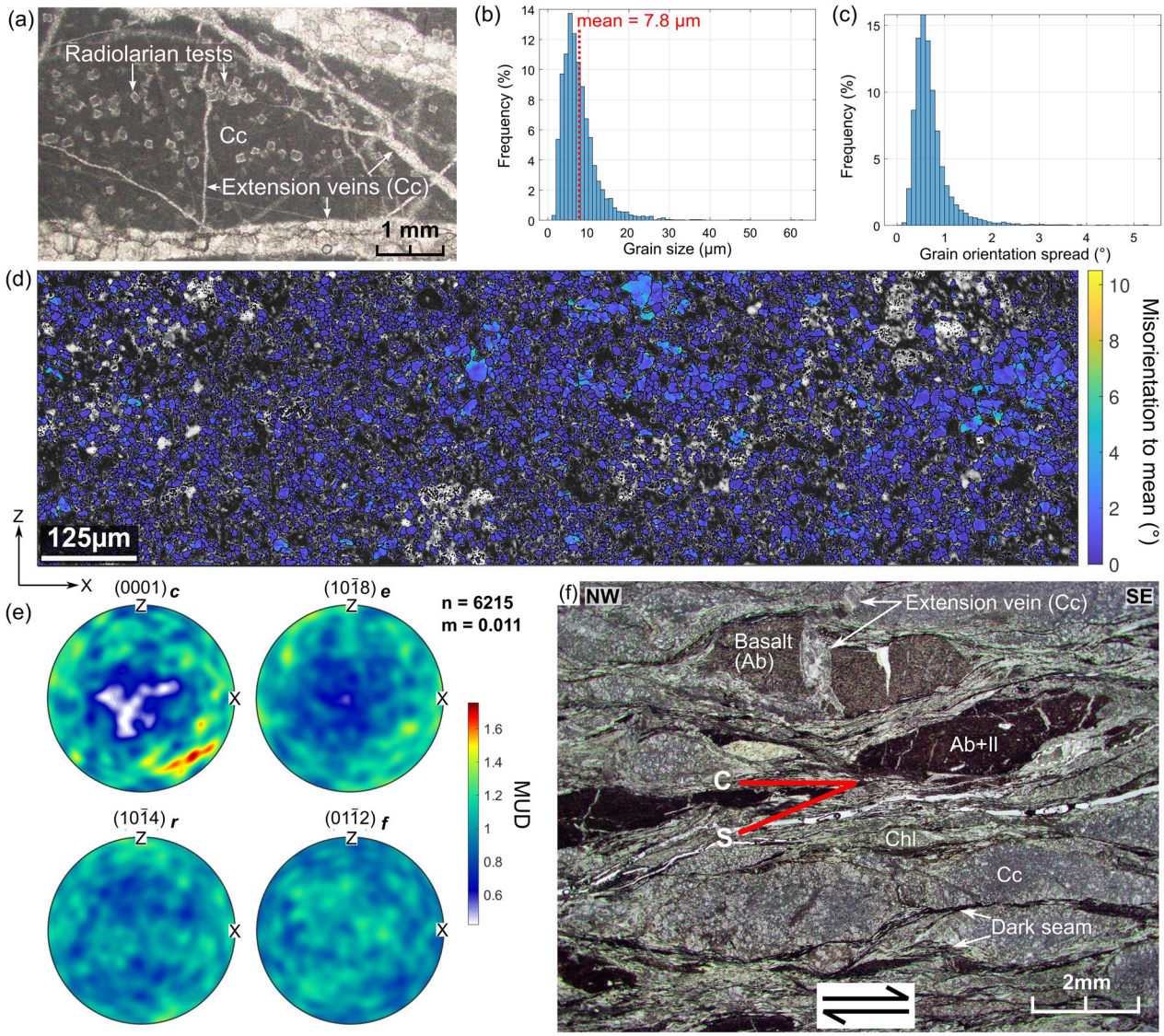

Fig. 5 Micritic limestone lenses in the BLM. Panels **b**–**e** were generated using MTEX software (Hielscher and Schaeben 2008; Mainprice et al. 2014). **a** Microcrystalline calcite (Cc) with radiolarian tests showing partial recrystallization to calcite. **b** Histogram of microcrystalline calcite grain size calculated from the diameter of reconstructed EBSD grains. **c** Histogram of grain orientation spread (GOS) of calcite, showing a low degree of intragranular misorientation. **d** GOS map of calcite on EBSD band contrast image of the micritic limestone. A given pixel within each of the calcite grains is colored by the angular degree of intragranular misorientation relative to the mean orientation of the parent grain. Most white grains correspond to chlorite and albite grains, identified by EBSD indexing and optical microscopy. Unindexed pixels are black. **e** CPO pole figures of microcrystalline calcite grains. CPO is plotted as equal-area, upper hemisphere projections. The crystal directions shown here were selected to examine the possibility of deformation under low-temperature calcite slip systems (De Bresser and Spiers 1997). The M-index (m) indicates that the fabric intensity is very weak (Skemer et al. 2005). Grains are plotted with the *X*-direction parallel to lineation and the *Z*-direction normal to foliation. *N* represents the number of measured points. **f** Micritic limestone (Cc) and basalt lenses in green chloritic matrix with *S*–*C* fabric showing top-to-SE shear sense. Dark seams contain Fe and Ti oxide minerals

observed adjacent to quartz and albite grains oriented parallel to the *S* surfaces (Fig. 7f).

Siliceous mudstone lenses contain minor amounts of phyllosilicates compared to the mudstone matrix. Sandstone lenses are composed of quartz and albite with a larger grain size (generally > 40 μm) and a relatively minor proportion of matrix dominated by illite. Similar to basalt lenses in the BLM, basalt lenses in the MDM are composed of fine-grained albite with abundant Fe–Ti oxide minerals and chlorite.

Raman spectra of carbonaceous material in the matrix of MDM show prominent peaks of the D1- and D2-bands

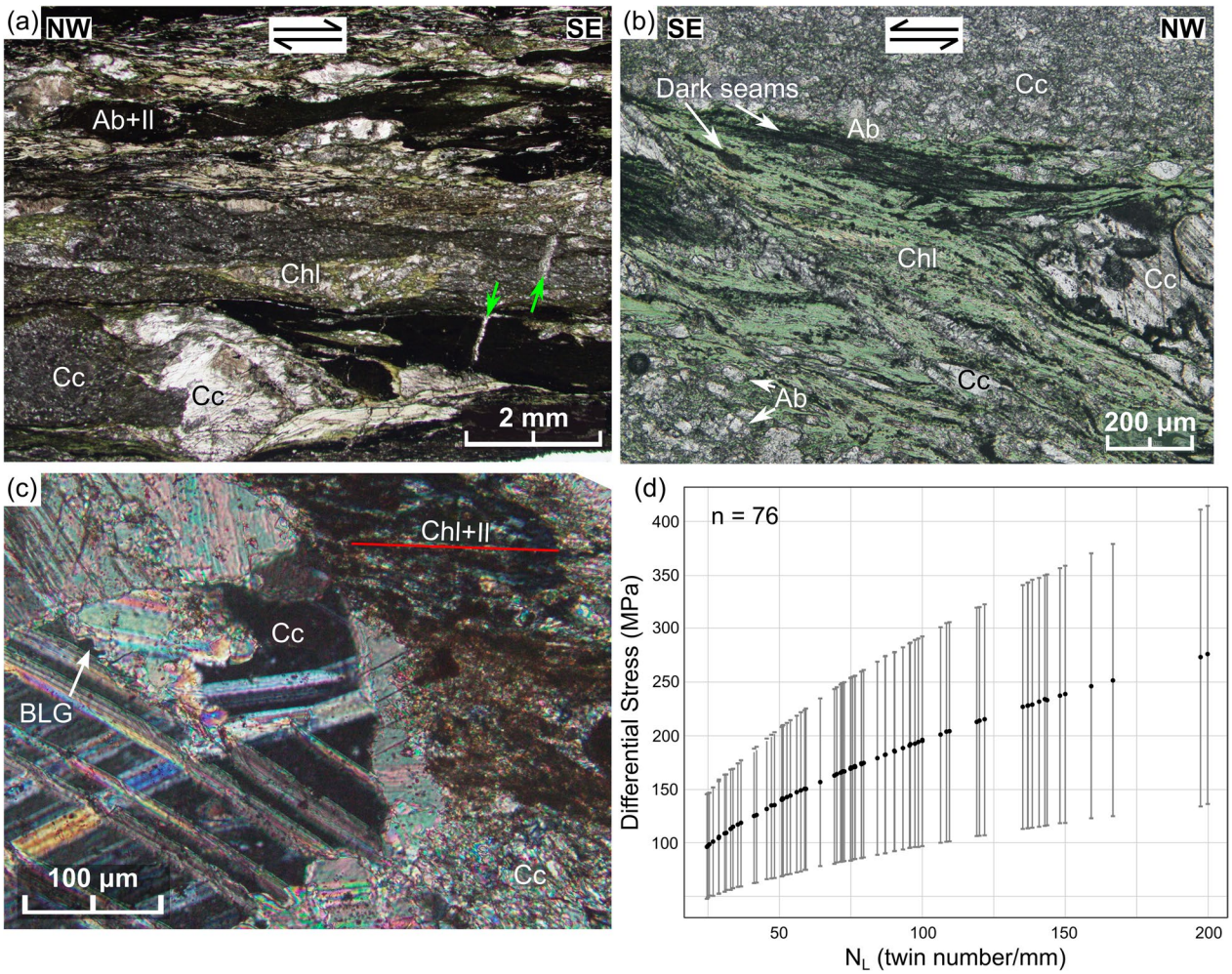

Fig. 6 Photomicrographs of coarse-grained calcite in the BLM. Panels **a** and **b** are plane-polarized light, panel c is cross-polarized light. **a** Coarse-grained calcite (Cc) is restricted to the margins of micritic limestone (Cc) lenses and extension veins. The extension vein at high angle to foliation (green arrows) is displaced by dark seams. **b** Close-up of the chlorite (Chl) matrix along the edge of a micritic limestone (Cc) lens. Dark seams are composed of iron (Fe), titanium (Ti), and illite (Il). **c** Thin section (cross-polarized light) with calcite showing type II (Burkhard 1993) twins. Bulging grain boundaries (BLG) can be observed at the contact between coarse calcite grains. **d** Average differential stress calculated from the e-twin density (N_L) paleopiezometer (Rybacki et al. 2013) of coarse-grained calcite. Individual data points represent the twin density of individual calcite grains

(Fig. 8a). The peak deformation temperatures, estimated from the full width at half maximum of the D1-band, are 281 ± 11 °C, 286 ± 12 °C, and 289 ± 12 °C (Fig. 8b, Supp. Info S1). The calculated uncertainties are smaller than the uncertainty of ± 30 °C inherent in the calibration (Kouketsu et al. 2014). The estimated temperatures are consistent with the occurrence of bulging recrystallization in MDM quartz veins at temperatures ≥ 280 °C (Stipp et al. 2002) and the development of type II calcite twins between 150 and 300 °C (Burkhard 1993) in BLM calcite veins.

5 Discussion

5.1 Deformation mechanisms of the mélanges

At macroscale, the scaly fabric of the MDM matrix is defined by anastomosing polished surfaces with slickenlines (Fig. 4a), indicating that deformation of the matrix was accommodated by frictional sliding of illite. However, under the microscope, pressure shadows are observed around quartz and albite grains in the matrix (Fig. 7f), and dark seams composed of illite with Ti and Fe oxide minerals likely represent zones of insoluble residue (Fig. 7a, f), consistent with deformation by pressure solution. Furthermore, stylolitized solid inclusion bands within crack-seal quartz veins (Fig. 7c) also indicate

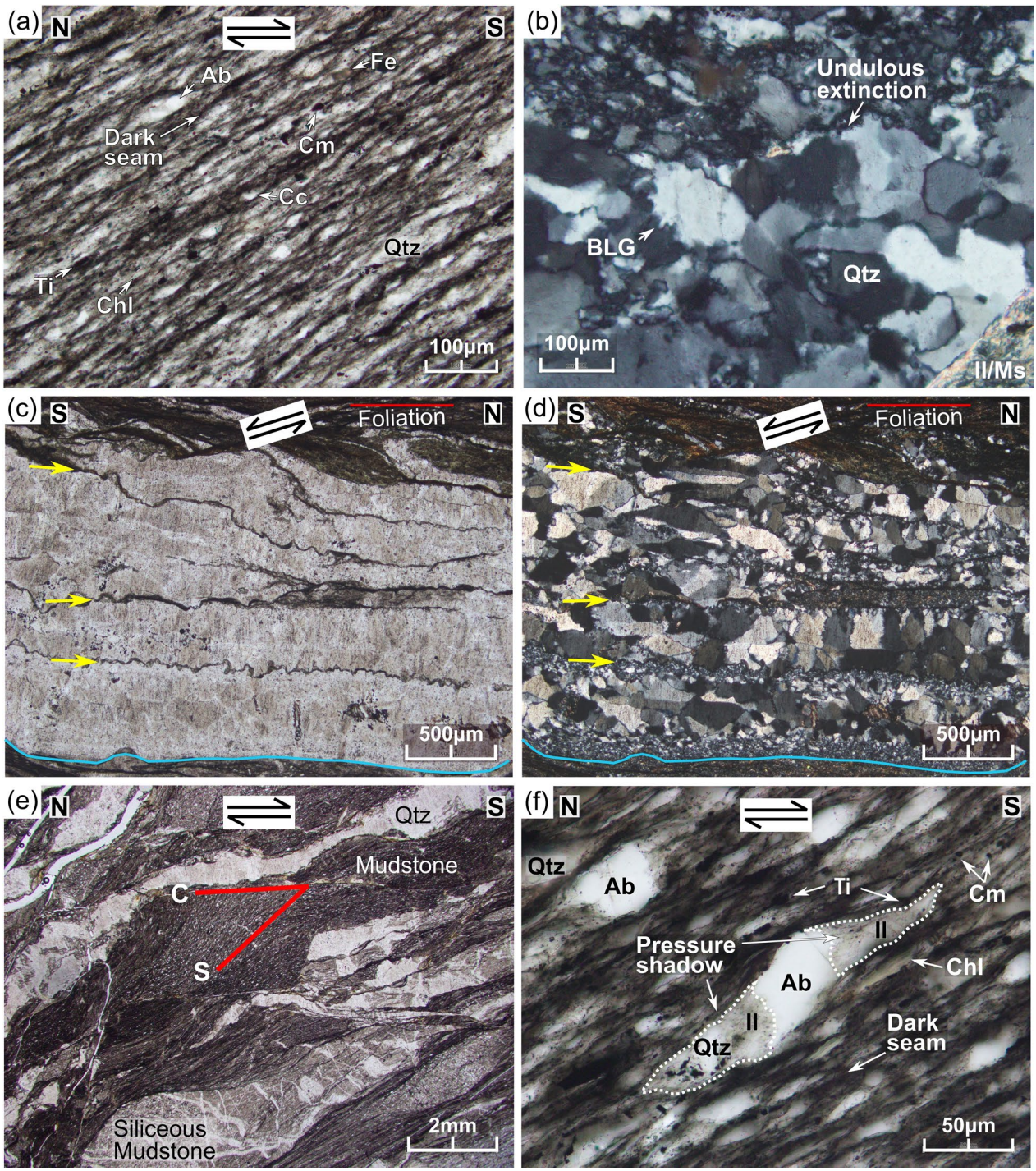

Fig. 7 Photomicrographs of the MDM. Panels **a**, **c**, **e**, and **f** are plane-polarized light, and panels **b** and **d** are cross-polarized light. **a** The mineral assemblage of the mudstone matrix consists of quartz (Qtz), albite (Ab), and rare calcite (Cc) grains in a matrix of illite (Il) with lesser chlorite (Chl). Dark seams contain titanium (Ti), iron (Fe) oxide minerals, and carbonaceous material (Cm). **b** Quartz grains from a foliation-parallel extension vein display bulging grain boundaries (BLG) and undulose extinction. **c** Photomicrograph (plane-polarized light) of a crack-seal extension vein parallel to foliation. Stylolitized phyllosilicate inclusion bands (yellow arrows) subparallel to the vein margin (blue line) indicate that the vein opened at a high angle to the vein margin. **d** Photomicrograph (cross-polarized light) of the crack-seal extension vein in panel c showing blocky quartz grain morphology. **e** *S–C* fabric showing top-to-SE shear sense. **f** Pressure shadow composed of quartz (Qtz) and illite (Il) around an albite (Ab) grain in the mudstone matrix

deformation by pressure solution. Quartz grains in the MDM exhibit undulose extinction and bulging grain boundaries (Fig. 7b), consistent with deformation by dislocation creep. The deformation and microstructural features of the MDM are therefore interpreted to represent the product of combined frictional sliding of illite and pressure solution creep of quartz (e.g., Bos and Spiers 2002), in conjunction with quartz dislocation creep.

In the BLM, polished surfaces with slickenlines (Fig. 3d) indicate deformation of the chloritic matrix by frictional sliding. At the microscopic scale, dark seams composed of Ti and Fe oxide minerals and illite (Fig. 6b) likely represent insoluble material associated with pressure solution. However, pressure shadows around limestone and basalt lenses and stylolites in calcite are not recognized. EDS mapping of limestone lenses shows no chemical zoning. The e-twinning and bulging grain boundaries in coarse-grained calcite in calcite extension veins (Fig. 6c) are indicative of intragranular deformation by dislocation climb and the onset of dynamic recrystallization (Burkhard 1993; Passchier and Trouw 2005; Lacombe et al. 2021). In contrast, the paucity of twins, limited intragranular deformation, and random CPO fabric (Fig. 5c–e) suggest that dislocation creep is not a dominant deformation mechanism for microcrystalline calcite in limestone lenses. Rather, the small size of the microcrystalline calcite could facilitate grain size-dependent diffusion mechanisms (Schmid et al. 1977; Walker et al. 1990; Hou et al. 2022; Ujiie et al. 2022). The deformation and microstructural features of the BLM are therefore interpreted to represent frictional sliding of chlorite and dislocation creep of coarse-grained calcite, with possible pressure solution creep in the BLM matrix and diffusion creep of fine-grained calcite in limestone lenses.

5.2 Origin of the mélanges

The BLM is characterized by the mixing of micritic limestone and basalt and does not contain terrigenous materials. Geochemical analyses indicated that basaltic lenses in the BLM were classified as ocean island basalt (OIB) (Motohashi et al. 2023b). The chloritic matrix in the BLM may be formed by alteration of basaltic glass on the seafloor or during subduction, as reported from basalt-bearing mélanges in exhumed accretionary complexes (Ujiie et al. 2007; Kameda et al. 2011; Phillips et al. 2020b; Leah et al. 2022). Motohashi et al. (2023b) and Osozawa et al. (2009) suggested that mixing of the OIB-derived basalt and micritic limestone above the seamount likely occurred prior to subduction during submarine landslides along the seamount flank. One possible location

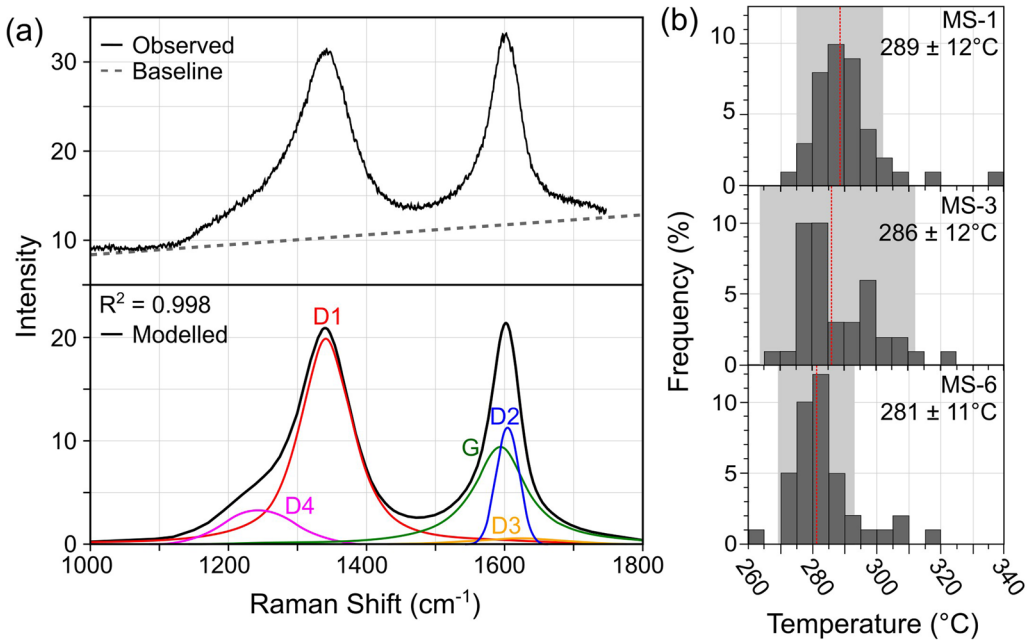

Fig. 8 Raman spectroscopic analysis of carbonaceous materials in the mudstone matrix of the MDM. **a** Representative Raman spectra of carbonaceous material (upper) and modeled spectra with decomposed peaks (lower). **b** Histograms showing the frequency distribution of temperature calculated using FWHM-D1 (Eq. 1) from 40 spot measurements of carbonaceous material. All data are shown in the histograms, but outliers greater than 2σ were excluded prior to calculation of the mean temperature. Dashed red lines and text indicate mean temperature and gray shaded regions show 2σ

for such mixing is at the foot of a steeply dipping fault scarp formed by normal faulting associated with oceanic plate bending in the outer rise region (e.g., Kobayashi et al. 1987; Taira et al. 1989). We also interpret the BLM as the result of a submarine landslide at the seamount margin (Fig. 9a).

OIB-derived basalt lenses are present in the MDM (Motohashi et al. 2023b), while terrigenous materials are absent from the BLM. The BLM lies above the MDM without a fault plane (Fig. 3b). The BLM overlying the MDM by isoclinal folding is unlikely due to the absence of the opposite stratigraphic/structural relationship (i.e., the MDM overlying the BLM) and the absence of a hinge zone (Fig. 2a). We therefore interpret that, while some OIB-derived basalt was incorporated into the trench-fill terrigenous sediments as lenses, there was no mixing between the trench-fill terrigenous sediments and the BLM during the juxtaposition of the BLM over the trench-fill terrigenous sediments by a submarine landslide (Fig. 9a).

Based on the absence of an asymmetric shear fabric and the presence of overlapping planar cleavages in the lenses of oceanic material, Osozawa et al. (2009) interpreted the mixing of terrigenous and oceanic materials to be due to debris flows from an older accreted oceanic material into trench-fill terrigenous sediments. However, both the BLM and the MDM preserve an asymmetric *S*–*C* fabric showing SE-directed shear consistent with megathrust shear (Figs. 3c, 4a, b). In addition, the foliations overprint both the BLM and the MDM (Fig. 3a). Thus, we suggest that the BLM was juxtaposed above the MDM by submarine landslide and then underwent subduction-related megathrust shear together to form a mélange shear zone. The mineral assemblage of basaltic rocks lacks epidote and actinolite, quartz grains show bulging recrystallization that becomes dominant at ~ 280 °C (Stipp et al. 2002) and undulose extinction (Fig. 7b), and Raman spectra of carbonaceous material give a peak temperature of ~ 281–289 °C (Fig. 8) suggesting that the mélange shear zone underwent sub-greenschist facies metamorphism (Fig. 9b).

5.3 Temporal changes in differential stress and fluid pressure

The extension veins in the sandstone and siliceous mudstone lenses generally develop at high angles to the foliation (Fig. 4b). Some extension veins penetrate both competent lenses and mudstone matrix, indicating that tensile fracturing persisted as the block-in-matrix fabric developed. Extension veins in boudinaged lenses and matrix foliation are commonly observed in subduction mélanges composed of sandstone lenses in mudstone matrix and are thought to be formed by layer-parallel extension under subvertical maximum principal stress (σ_1) during subduction (Fisher and Byrne 1987; Ujiie 2002). Similarly, the extension veins at high angles to the foliation in the MDM are thought to form during subduction.

Extension veins parallel to foliation suggest rotation of σ_1 from sub-perpendicular to parallel to foliation. Solid inclusion bands subparallel to vein margins indicate repeated fracturing and silica precipitation. These features suggest repeated generation of near-lithostatic fluid pressures. Sigmoidal deformation of foliation-parallel veins with top-to-SE shear sense indicates that viscous shear by pressure solution creep occurred after tensile failure under near-lithostatic fluid pressures (Fig. 4f). The stylolitized solid inclusion bands also suggest that deformation by pressure solution creep during which σ_1 rotated to perpendicular to the *S* surface followed repeated tensile failure under near-lithostatic fluid pressure (Fig. 7c). Quartz-filled shear veins parallel to the *C* surfaces truncate sigmoidal fabrics, likely representing dilational shear at lower differential stress and higher fluid pressure than viscous shear by pressure solution creep (Fig. 9c).

In contrast to the MDM, quartz veins are not observed at the outcrop scale in the BLM, in part due to the low silica content of the basaltic and limestone rocks. At the microscopic scale, the calcite-filled extension veins at high angles to the foliation are displaced along shear surfaces in the matrix (Fig. 6a), while calcite-filled extension and shear veins at low angles to the foliation are rarely observed (Fig. 9c). Fewer veins in the BLM relative to the MDM could represent lower fluid pressures and/or higher strength of the BLM relative to the MDM. For example, the tensile strength of limestone (T_0 = 5–25 MPa; Winkler 1997) and basalt (T_0 = 10–30 MPa; Winkler 1997) is greater than that of pelitic rock (T_0 = 1 MPa; Lockner 1995). Another possibility for fewer veins in the BLM is a decrease in calcite solubility (Weyl 1959) at temperatures of ~ 281–289 °C under sub-greenschist facies metamorphic conditions.

Calcite twins formed by dislocation creep in the BLM record σ_d of 97–276 MPa (Fig. 6d), comparable to σ_d of 30–255 MPa from calcite twinning in chloritic Gwana mélange (Leah et al. 2022). Dislocation creep of quartz and combined pressure solution creep with frictional sliding of phyllosilicates in the MDM are favored at lower fluid pressure and higher σ_d. In contrast, considering T_0 = 1 MPa (Lockner 1995), foliation-parallel extension veins and shear veins in the MDM can develop at $\sigma_d = 4$ and $4 < \sigma_d < 5.66$ MPa, respectively (Secor 1965). Therefore, the mélange shear zone, at least the MDM, records temporal changes in σ_d, and fluid pressure.

Foliation-parallel veins suggest σ_1 parallel to the mélange shear zone. Such a stress field is likely downdip

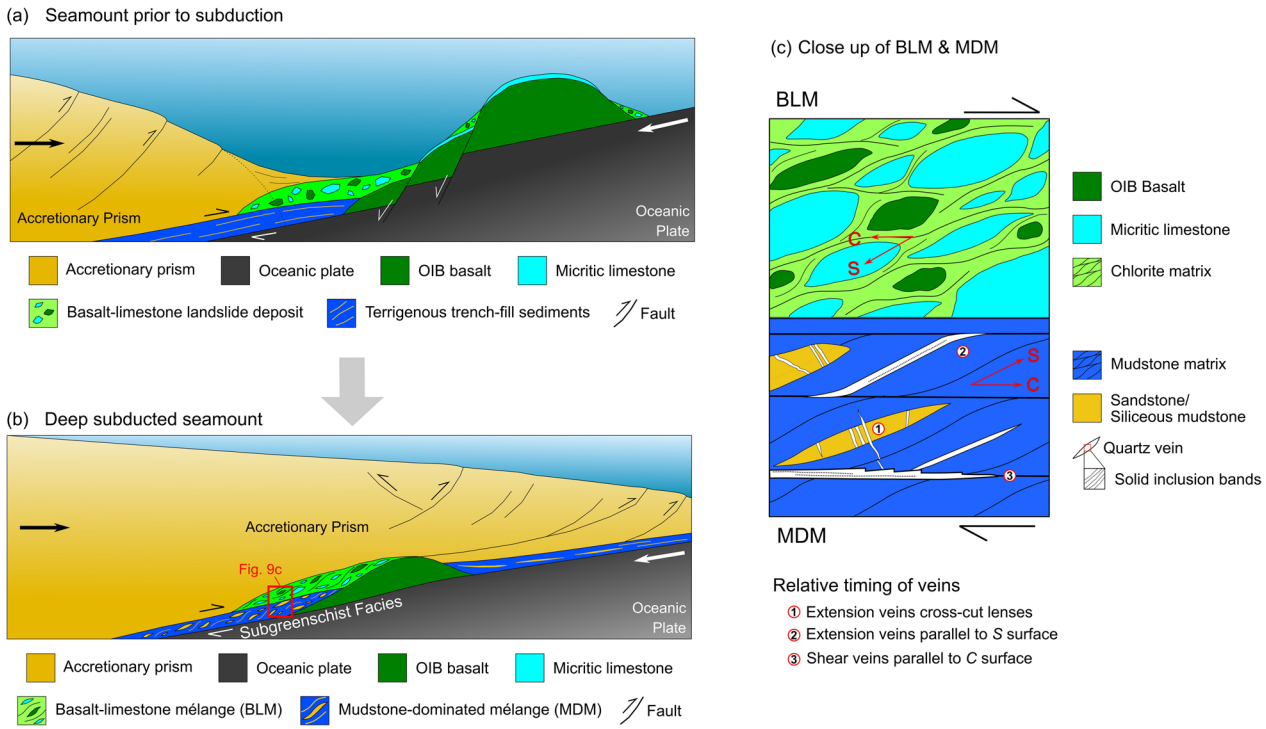

Fig. 9 Schematics showing the development of the BLM and MDM as a result of seamount subduction. **a** A seamount composed of OIB basalt (dark green) capped by micritic limestone (light blue) entering a subduction zone. The landward edge of the seamount may be displaced by normal faults accommodating plate flexure at the outer rise region. A submarine landslide at the steeply dipping normal fault scarps results in mixing of micritic limestone and OIB basalt and deposition above terrigenous trench-fill sediments. **b** The basalt–limestone deposit and terrigenous trench-fill sediments are subducted to sub-greenschist facies metamorphic conditions and form megathrust shear zones downdip of a subduction seamount, resulting in the formation of the BLM and MDM. **c** Deformation features in the BLM and MDM showing an *S*–*C* fabric. The BLM is characterized by OIB basalt (dark green) and micritic limestone (light blue) lenses wrapped by the chloritic matrix (light green). The MDM is represented by sandstone and siliceous mudstone lenses (yellow) surrounded by the illitic matrix (blue) and records progressive quartz vein formation

of the subducting seamount, where tectonic compression is enhanced, rather than updip, where extension in the wake of the subducting seamount is expected (Sun et al. 2020; Bangs et al. 2023; Gase et al. 2023). The clustered quartz veins in the subducting rocks are thought to represent a geological fingerprint of the tremor (Fagereng et al. 2011; Ujiie et al. 2018, 2024; Giuntoli et al. 2022). The brittle deformation under near-lithostatic fluid pressure recorded in the quartz-filled extension and shear veins may also represent tremorgenic deformation in the megathrust-related shear zones downdip of a subducting seamount, as observed in the northern Hikurangi subduction zone (Todd and Schwartz 2016; Todd et al. 2018; Barnes et al. 2020). In addition to tremor, slow slip events are observed downdip of a subducted seamount (Nishimura 2014; Collot et al. 2017; Barker et al. 2018; Todd et al. 2018). Viscous shear in the MDM is accommodated by combined pressure solution creep with frictional sliding of illite in conjunction with quartz dislocation creep. Stress greater than 100 MPa is required for pressure solution creep in metasedimentary rocks to accommodate slow slip strain rates (Condit and French 2022). This suggests that slow slip accommodated by viscous shear is unrealistic in the MDM. Leah et al. (2022) show that frictional sliding of chlorite at elevated fluid pressure may accommodate slow slip. This may be comparable to the viscous shear in the BLM that was accommodated by frictional sliding of chlorite. However, evidence for elevated fluid pressure is generally lacking in the BLM.

6 Conclusions

We examined the lithology, deformation mechanisms, and fluid conditions of the mélange shear zones formed in association with the subduction of a seamount. The mélange shear zones are composed of basalt–limestone mélange (BLM) originating from the mixing of limestone and basalt at the foot of a seamount and mudstone-dominated mélange (MDM) derived from the terrigenous sediments. The juxtaposition of the BLM over the MDM

occurred by submarine landslide from the seamount to trench-fill terrigenous sediments. The mineral assemblage of basaltic rocks, quartz grains with bulging grain boundaries and undulose extinction, and a peak temperature of ~ 281–289 °C determined by Raman spectra of carbonaceous material suggest that the mélange shear zones were deformed under sub-greenschist facies metamorphism. The deformation mechanisms of the BLM are frictional sliding of chlorite and dislocation creep of coarse-grained calcite, possibly accompanied by diffusion creep of very fine-grained calcite, whereas the MDM was deformed under the operation of dislocation creep of quartz and combined quartz pressure solution and frictional sliding of illite. The MDM records temporal changes in differential stress and fluid pressure downdip of a subducting seamount; quartz-filled shear and extension veins formed during periods of very low differential stress and near-lithostatic fluid pressure, while dislocation creep and pressure solution creep combined with frictional sliding of illite operated under higher differential stress and lower fluid pressure. The brittle deformation under very low differential stress and near-lithostatic fluid pressure may represent tremor downdip of a subducting seamount. However, viscous shear in the MDM and BLM under higher differential stress and lower fluid pressure is unlikely to accommodate slow slip events.

Abbreviations

σ	Standard deviation
σ_1	Maximum principle stress
σ_d	Differential stress
BLM	Basalt–limestone mélange
CPO	Crystallographic preferred orientation
EBSD	Electron backscatter diffraction
EDS	Energy-dispersive X-ray spectroscopy
FWHM-D1	Full width at half maximum of the D1-band
GOS	Grain orientation spread
MAD	Mean angular deviation
MDM	Mudstone-dominated mélange
N_L	Number of twins per mm
OIB	Ocean island basalt
SEM	Scanning electron microscopy
SSE	Slow slip event
T_0	Tensile strength

Supplementary Information

The online version contains supplementary material available at https://doi.org/10.1186/s40645-024-00641-y.

Additional file 1.

Acknowledgements

We would like to thank the Amami Gunto National Park Management Office (Amami Wildlife Conservation Center) of the Ministry of the Environment for permission to sample at Asanzaki, Y. Kouketsu for their analytical support of Raman analysis, T. Sano for review of geochemical interpretations, S. Wallis for providing the EBSD system at the University of Tokyo, Y. Yamasaki for field assistance, and N. Nishiyama for both field assistance and critical discussion of our results. Constructive comments from T. Byrne, P. Vannucchi, A. Fagereng, and an anonymous reviewer significantly improved the manuscript.

Author contributions

M.F. and K.U. conceptualized the study, the methodology was determined by M.F., K.U., and T.N. K.U. obtained funding and supervised the project. M.F., K.U., and G.M. contributed to fieldwork and, in collaboration with T.N., data acquisition and investigation. M.F. wrote the manuscript and all authors contributed to the review and editing process and visualization.

Funding

This project was supported by funding from the Japan Society for the Promotion of Science (JSPS) KAKENHI Grants JP16H06476, 20K21050, 20KK0078, and 21H05203 to KU.

Availability of data and materials

Results of the Raman spectra analysis are available in Supplementary Information. The datasets supporting the conclusions of this article including structural measurements, Raman spectra, and EBSD data, are available in the Open Science Framework repository, https://osf.io/ydbha/. Code for R Project for Statistical Computing (R Core Team 2021) v4.1.0 with RStudio v2022.07.1+554 (used for calculation of Raman temperature and plot generation) and MATLAB R2022a with the MTEX (Mainprice et al. 2014) v5.8.2 toolbox (EBSD analysis) is available from the GitHub repository, https://github.com/madisonfrank/Asanzaki_DeformationMechanisms.

Declarations

Competing interests

The authors declare that they have no competing interests.

Received: 27 November 2023 Accepted: 10 June 2024
Published online: 17 June 2024

References

Ando R, Ujiie K, Nishiyama N, Mori Y (2023) Depth-dependent slow earthquakes controlled by temperature dependence of brittle-ductile transitional rheology. Geophys Res Lett 50(5):e2022GL101388. https://doi.org/10.1029/2022GL101388

Bangs NL, Morgan JK, Bell RE, Han S, Arai R, Kodaira S, Gase AC, Wu X, Davy R, Frahm L, Tilley HL, Barker DHN, Edwards JH, Tobin HJ, Reston TJ, Henrys SA, Moore GF, Bassett D, Kellett R, Stucker V, Fry B (2023) Slow slip along the Hikurangi margin linked to fluid-rich sediments trailing subducting seamounts. Nat Geosci. https://doi.org/10.1038/s41561-023-01186-3

Barbero E, Di Rosa M, Pandolfi L, Delavari M, Dolati A, Zaccarini F, Saccani E, Marroni M (2023) Deformation history and processes during accretion of seamounts in subduction zones: the example of the Durkan Complex (Makran, SE Iran). Geosci Front 14:101522. https://doi.org/10.1016/j.gsf.2022.101522

Barker DH, Henrys S, Caratori Tontini F, Barnes PM, Bassett D, Todd E, Wallace L (2018) Geophysical constraints on the relationship between seamount subduction, slow slip, and tremor at the north Hikurangi subduction zone, New Zealand. Geophys Res Lett 45:12–804. https://doi.org/10.1029/2018GL080259

Barnes PM, Wallace LM, Saffer DM, Bell RE, Underwood MB, Fagereng A, Meneghini F, Savage HM, Rabinowitz HS, Morgan JK, Kitajima H, Kutterolf S, Hashimoto Y, Engelmann de Oliveira CH, Noda A, Crundwell MP, Shepherd CL, Woodhouse AD, Harris RN, Wang M, Henrys S, Barker DHN, Petronotis KE, Bourlange SM, Clennell MB, Cook AE, Dugan BE, Elger J, Fulton PM, Gamboa D et al (2020) Slow slip source characterized by lithological and geometric heterogeneity. Sci Adv 6:eaay3314. https://doi.org/10.1126/sciadv.aay3314

Bonnet G, Agard P, Angiboust S, Monie P, Fournier M, Caron B, Omrani J (2020) Structure and metamorphism of a subducted seamount (Zagros suture, Southern Iran). Geosphere 16:62–81. https://doi.org/10.1130/GES02134.1

Bos B, Spiers CJ (2002) Frictional-viscous flow of phyllosilicate-bearing fault rock: microphysical model and implications for crustal strength profiles. J Geophys Res Solid Earth 107:ECV-1. https://doi.org/10.1029/2001JB000301

Burkhard M (1993) Calcite twins, their geometry, appearance and significance as stress-strain markers and indicators of tectonic regime: a review. J Struct Geol 15:351–368. https://doi.org/10.1016/0191-8141(93)90132-T
Collot J-Y, Sanclemente E, Nocquet J-M, Leprêtre A, Ribodetti A, Jarrin P, Chlieh M, Graindorge D, Charvis P (2017) Subducted oceanic relief locks the shallow megathrust in central Ecuador. J Geophys Res Solid Earth 122:3286–3305. https://doi.org/10.1002/2016JB013849
Condit C, French M (2022) Geologic evidence of lithostatic pore fluid pressures at the base of the subduction seismogenic zone. Geophys Res Lett 49:e2022GL098862. https://doi.org/10.1029/2022GL098862
De Bresser J, Spiers C (1997) Strength characteristics of the r, f, and c slip systems in calcite. Tectonophysics 272:1–23. https://doi.org/10.1016/S0040-1951(96)00273-9
Eggleston RA, Bailey SW (1967) Structural aspects of dioctahedral chlorite. Am Mineral 52:673–689
Fagereng Å (2011) Geology of the seismogenic subduction thrust interface. Geol Soc Lond Spec Publ 359:55–76. https://doi.org/10.1144/SP359.4
Fagereng Å, Beall A (2021) Is complex fault zone behaviour a reflection of rheological heterogeneity? Philos Trans R Soc A 379:20190421. https://doi.org/10.1098/rsta.2019.0421
Fagereng Å, Remitti F, Sibson RH (2011) Incrementally developed slickenfibers—Geological record of repeating low stress-drop seismic events? Tectonophysics 510:381–386. https://doi.org/10.1016/j.tecto.2011.08.015
Fisher D, Byrne T (1987) Structural evolution of underthrusted sediments, Kodiak Islands, Alaska. Tectonics 6:775–793. https://doi.org/10.1029/TC006i006p00775
Gase AC, Bangs NL, Saffer DM, Han S, Miller PK, Bell RE, Arai R, Henrys SA, Kodaira S, Davy R, Frahm L, Barker DHN (2023) Subducting volcaniclastic-rich upper crust supplies fluids for shallow megathrust and slow slip. Sci Adv 9:eadh0150. https://doi.org/10.1126/sciadv.adh0150
Giuntoli F, Viola G, Sørensen BE (2022) Deformation mechanisms of blueschist facies continental metasediments may offer insights into deep episodic tremor and slow slip events. J Geophys Res Solid Earth 127:e2022JB024265. https://doi.org/10.1029/2022JB024265
Harris R, Sakaguchi A, Petronotis K, Baxter A, Berg R, Burkett A, Charpentier D, Choi J, Ferreiro PD, Hamahashi M, Hashimoto Y, Heydolph K, Jovane L, Kastner M, Kurz W, Kutterolf SO, Li Y, Malinverno A, Martin KM, Millan C, Nascimento DB, Saito S, Sandoval Gutierrez MI, Screaton EJ, Smith-Duque CE, Solomon EA, Straub SM, Tanikawa W, Torres ME, Uchimura H, et al. (2013) Expedition 344 summary. In: Proceedings of IODP 344:2. https://doi.org/10.2204/iodp.proc.344.101.2013
Heuret A, Conrad C, Funiciello F, Lallemand S, Sandri L (2012) Relation between subduction megathrust earthquakes, trench sediment thickness and upper plate strain. Geophys Res Lett. https://doi.org/10.1029/2011GL050712
Hielscher R, Schaeben H (2008) A novel pole figure inversion method: specification of the MTEX algorithm. J Appl Crystallogr 41:1024–1037. https://doi.org/10.1107/S0021889808030112
Hou C, Liu J, Zheng Y, Sun Y, Zhou B, Fan W (2022) Prolonged grain boundary sliding in naturally deformed calcite marble at the middle crustal level. J Struct Geol 161:104658. https://doi.org/10.1016/j.jsg.2022.104658
Ishikawa H, Yamakuchi S (1965) On the discovery of ammonite from Honto Isl. of Amami-Oshima and its geological meaning. J Geol Soc Jpn 71:78–79. https://doi.org/10.5575/geosoc.71.78
Kameda J, Ujiie K, Yamaguchi A, Kimura G (2011) Smectite to chlorite conversion by frictional heating along a subduction thrust. Earth Planet Sci Lett 305:161–170. https://doi.org/10.1016/j.epsl.2011.02.051
Kanisawa S, Osozawa S, Nakagawa H (1983) Petrology of Mesozoic lamprophyres in Amami-Oshima, Kagoshima Prefecture, Japan. J Japan Assoc Mineral Petrol Econ Geol 78:394–404. https://doi.org/10.2465/ganko1941.78.394
Kobayashi K, Cadet J-P, Aubouin J, Boulègue J, Dubois J, von Huene R, Jolivet L, Kanazawa T, Kasahara J, Koizumi K, Lallemand S, Nakamura Y, Pautot G, Suyehiro K, Tani S, Tokuyama H, Yamazaki T (1987) Normal faulting of the Daiichi-Kashima Seamount in the Japan Trench revealed by the Kaiko I cruise, Leg 3. Earth Planet Sci Lett 83:257–266. https://doi.org/10.1016/0012-821X(87)90070-7
Kouketsu Y, Mizukami T, Mori H, Endo S, Aoya M, Hara H, Nakamura D, Wallis S (2014) A new approach to develop the Raman carbonaceous material geothermometer for low-grade metamorphism using peak width. Isl Arc 23:33–50. https://doi.org/10.1111/iar.12057
Lacombe O, Parlangeau C, Beaudoin NE, Amrouch K (2021) Calcite twin formation, measurement and use as stress–strain indicators: a review of progress over the last decade. Geosci J 11:445. https://doi.org/10.3390/geosciences11110445
Leah H, Fagereng Å, Groome N, Buchs D, Eijsink A, Niemeijer A (2022) Heterogeneous subgreenschist deformation in an exhumed sediment-poor mélange. J Geophys Res Solid Earth. https://doi.org/10.1029/2022JB024353
Lockner DA (1995) Rock failure. In: Ahrens TJ (ed) Rock physics & phase relations: a handbook of physical constants. AGU Ref Shelf 3:127–147, 1st edn. American Geophysical Union, Washington. https://doi.org/10.1029/RF003
Mainprice D, Bachmann F, Hielscher R, Schaeben H (2014) Descriptive tools for the analysis of texture projects with large datasets using MTEX: strength, symmetry and components. Geol Soc Lond Spec Publ 409:251–271
Matsumoto T, Ishikawa H, Yamakuchi S (1966) A Mesozoic ammonite from Amami-Oshima. Trans Proc Paleontol Soc Jpn New Ser 62:234–241. https://doi.org/10.14825/prpsj1951.1966.62_234. (**in Japanese**)
Matsuoka A (1992) Jurassic-Early Cretaceous tectonic evolution of the Southern Chichibu terrane, southwest Japan. Palaeogeogr Palaeoclimatol Palaeoecol 96:71–88. https://doi.org/10.1016/0031-0182(92)90060-I
Motohashi G, Ishizuka O, Oda H, Sano T, Sekimoto S, Ujiie K (2023a) Middle Miocene forearc alkaline magmatism in Amami-Oshima Island, central Ryukyu Arc: implications for paleoreconstruction of Shikoku Basin. Earth Planets Space 75:1–14. https://doi.org/10.1186/s40623-022-01760-w
Motohashi G, Sano T, Ujiie K, Frank M (2023b) Origin of alkaline basaltic intrusive rocks in an exhumed accretionary complex: implications for past petit-spot volcanism in the ocean. Geochem Geophys Geosys 24(4):e2022GC010801. https://doi.org/10.1029/2022GC010801
Nagaya T, Wallis SR, Seto Y, Miyake A, Soda Y, Uehara S, Matsumoto M (2017) Minimizing and quantifying mis-indexing in electron backscatter diffraction (EBSD) determinations of antigorite crystal directions. J Struct Geol 95:127–141. https://doi.org/10.1016/j.jsg.2016.12.006
Nishikawa T, Matsuzawa T, Ohta K, Uchida N, Nishimura T, Ide S (2019) The slow earthquake spectrum in the Japan Trench illuminated by the S-net seafloor observatories. Science 365:808–813. https://doi.org/10.1126/science.aax5618
Nishimura T (2014) Short-term slow slip events along the Ryukyu Trench, southwestern Japan, observed by continuous GNSS. Prog Earth Planet Sci 1:1–13. https://doi.org/10.1186/s40645-014-0022-5
Norabuena E, Dixon TH, Schwartz S, DeShon H, Newman A, Protti M, Gonzalez V, Dorman L, Flueh ER, Lundgren P, Pollitz F, Sampson D (2004) Geodetic and seismic constraints on some seismogenic zone processes in Costa Rica. J Geophys Res Solid Earth. https://doi.org/10.1029/2003JB002931
Osozawa S (1984) Geology of Amami Oshima, central Ryukyu Islands, with special reference to effect of gravity transportation on geologic structure. Tohoku Univ Sci Rep, 2nd Ser (geol) 54(2):165–189 (**ISSN: 0082464X**)
Osozawa S, Morimoto J, Flower MF (2009) "Block-in-matrix" fabrics that lack shearing but possess composite cleavage planes: a sedimentary mélange origin for the Yuwan accretionary complex in the Ryukyu island arc, Japan. Geol Soc Am Bull 121:1190–1203. https://doi.org/10.1130/B26038.1
Outerbridge KC, Dixon TH, Schwartz SY, Walter JI, Protti M, Gonzalez V, Biggs J, Thorwart M, Rabbel W (2010) A tremor and slip event on the Cocos-Caribbean subduction zone as measured by a global positioning system (GPS) and seismic network on the Nicoya Peninsula, Costa Rica. J Geophys Res Solid Earth. https://doi.org/10.1029/2009JB006845
Paquette J, Reeder RJ (1990) Single-crystal X-ray structure refinements of two biogenic magnesian calcite crystals. Am Mineral 75:1151–1158 (**ISSN: 0003-004X**)
Passchier CW, Trouw RA (2005) Microtectonics, 2nd edn. Springer, Berlin. https://doi.org/10.1007/3-540-29359-0
Phillips NJ, Belzer B, French ME, Rowe CD, Ujiie K (2020a) Frictional strengths of subduction thrust rocks in the region of shallow slow earthquakes. J Geophys Res Solid Earth 125:e2019JB018888. https://doi.org/10.1029/2019JB018888
Phillips NJ, Motohashi G, Ujiie K, Rowe CD (2020b) Evidence of localized failure along altered basaltic blocks in tectonic mélange at the updip limit of the seismogenic zone: implications for the shallow slow earthquake source. Geochem Geophys Geosys 21(7):e2019GC008839. https://doi.org/10.1029/2019GC008839

R Core Team (2021) R: a language and environment for statistical computing. https://www.R-project.org/
Rybacki E, Evans B, Janssen C, Wirth R, Dresen G (2013) Influence of stress, temperature, and strain on calcite twins constrained by deformation experiments. Tectonophysics 601:20–36. https://doi.org/10.1016/j.tecto.2013.04.021
Schmid S, Boland J, Paterson M (1977) Superplastic flow in finegrained limestone. Tectonophysics 43:257–291. https://doi.org/10.1016/0040-1951(77)90120-2
Secor DT (1965) Role of fluid pressure in jointing. Am J Sci 263:633–646. https://doi.org/10.2475/ajs.263.8.633
Shibata K, Nozawa T (1966) K-Ar ages of granites from Amami-oshima, Ryukyu Islands, Japan. Bull Geol Surv Jpn 17:430–435
Skemer P, Katayama I, Jiang Z, Karato S (2005) The misorientation index: development of a new method for calculating the strength of lattice-preferred orientation. Tectonophysics 411:157–167. https://doi.org/10.1016/j.tecto.2005.08.023
Stipp M, StuĚnitz H, Heilbronner R, Schmid SM (2002) The eastern Tonale fault zone: a "natural laboratory" for crystal plastic deformation of quartz over a temperature range from 250 to 700 C. J Struct Geol 24:1861–1884. https://doi.org/10.1016/S0191-8141(02)00035-4
Sun T, Saffer D, Ellis S (2020) Mechanical and hydrological effects of seamount subduction on megathrust stress and slip. Nat Geosci 13:249–255. https://doi.org/10.1038/s41561-020-0542-0
Taira A, Tokuyama H, Soh W (1989) Accretion tectonics and evolution of Japan. In: Ben-Avraham Z (ed) The evolution of the Pacific Ocean margin. Oxford monographs on geology and geophysics, vol 8. Oxford University Press, New York, pp 100–123
Taira A, Ohara Y, Wallis S, Ishiwatari A, Iryu Y, Moreno T (2016) Geological evolution of Japan: an overview. In: Moreno T, Wallis S, Kojima T, Gibbons W (eds) The geology of Japan. Geological Society London, London, pp 1–24. https://doi.org/10.1144/GOJ.1
Takeuchi M (1993) Geology of the Yuwan district. With Geological Sheet Map at 1:50,000. Geological Survey of Japan, p 69. (**in Japanese**)
Tilley H, Moore G, Underwood M, Hernández-Molina F, Yamashita M, Kodaira S, Nakanishi A (2021) Heterogeneous sediment input at the Nankai Trough subduction zone: implications for shallow slow earthquake localization. Geochem Geophys Geosyst 22(10):e2021GC009965. https://doi.org/10.1029/2021GC009965
Todd EK, Schwartz SY (2016) Tectonic tremor along the northern Hikurangi Margin, New Zealand, between 2010 and 2015. J Geophys Res Solid Earth 121:8706–8719. https://doi.org/10.1002/2016JB013480
Todd EK, Schwartz SY, Mochizuki K, Wallace LM, Sheehan AF, Webb SC, Williams CA, Nakai J, Yarce J, Fry B, Henrys S, Ito Y (2018) Earthquakes and tremor linked to seamount subduction during shallow slow slip at the Hikurangi margin, New Zealand. J Geophys Res Solid Earth 123:6769–6783. https://doi.org/10.1029/2018JB016136
Tonegawa T, Yamashita Y, Takahashi T, Shinohara M, Ishihara Y, Kodaira S, Kaneda Y (2020) Spatial relationship between shallow very low frequency earthquakes and the subducted Kyushu-Palau Ridge in the Hyuga-nada region of the Nankai subduction zone. Geophys J Int 222:1542–1554. https://doi.org/10.1093/gji/ggaa264
Ujiie K (2002) Evolution and kinematics of an ancient décollement zone, mélange in the Shimanto accretionary complex of Okinawa Island, Ryukyu Arc. J Struct Geol 24:937–952. https://doi.org/10.1016/S0191-8141(01)00103-1
Ujiie K, Yamaguchi A, Kimura G, Toh S (2007) Fluidization of granular material in a subduction thrust at seismogenic depths. Earth Planet Sci Lett 259:307–318. https://doi.org/10.1016/j.epsl.2007.04.049
Ujiie K, Saishu H, Fagereng Å, Nishiyama N, Otsubo M, Masuyama H, Kagi H (2018) An explanation of episodic tremor and slow slip constrained by crack-seal veins and viscous shear in subduction mélange. Geophys Res Lett 45:5371–5379. https://doi.org/10.1029/2018GL078374
Ujiie K, Noro K, Shigematsu N, Fagereng Å, Nishiyama N, Tulley CJ, Masuyama H, Mori Y, Kagi H (2022) Megathrust shear modulated by albite metasomatism in subduction mélanges. Geochem Geophys Geosyst 23(8):e2022GC010569. https://doi.org/10.1029/2022GC010569
Ujiie K, Nishiyama N, Yamamoto H, Yamashita M, Nagaya T, Sano T, Kouketsu Y (2024) Duplex underplating, sediment dehydration and quartz vein mineralization in the deep tremor source region. J Geophys Res Solid Earth 129:e2023JB027901. https://doi.org/10.1029/2023JB027901
Vannucchi P, Clarke A, de Montserrat A, Ougier-Simonin A, Aldega L, Morgan JP (2022) A strength inversion origin for non-volcanic tremor. Nat Commun 13:1–13. https://doi.org/10.1038/s41467-022-29944-8
Walker A, Rutter E, Brodie K (1990) Experimental study of grain-size sensitive flow of synthetic, hot-pressed calcite rocks. Geol Soc Lond Spec Publ 54:259–284. https://doi.org/10.1144/GSL.SP.1990.054.01.24
Wallis SR, Yamaoka K, Mori H, Ishiwatari A, Miyazaki K, Ueda H (2020) The basement geology of Japan from A to Z. Island Arc 29:e12339. https://doi.org/10.1111/iar.12339
Wang K, Bilek SL (2014) Fault creep caused by subduction of rough seafloor relief. Tectonophysics 610:1–24. https://doi.org/10.1016/j.tecto.2013.11.024
Weyl PK (1959) Pressure solution and the force of crystallization: a phenomenological theory. J Geophys Res 64:2001–2025. https://doi.org/10.1029/JZ064i011p02001
Winkler E (1997) Stone in architecture: properties, durability, 3rd edn. Springer, Berlin. https://doi.org/10.1007/978-3-662-10070-7

Publisher's Note